JMEPEG
https://doi.org/10.1007/s11665-024-09881-x

1059-9495/$19.00

ORIGINAL RESEARCH ARTICLE

The Process of Steam Oxidation Degradation of High Cr Steel after 125 000 Hours at 568 °C under 16.5 MPa

Tomasz Dudziak, Jerzy Morgiel, Grzegorz Golański, Puneet Chandran, Karolina Chat-Wilk, and Adelajda Polkowska

Submitted: 29 February 2024 / Revised: 30 April 2024 / Accepted: 15 May 2024

The aim of this work was to analyze the effect of steam oxidation when TP347HFG grade steel was exposed to industrial conditions for 125 000 hrs at 568 °C under 16.5 MPa pressure. The testing material was acquired from one of the coal power plants operating in Poland. Comprehensive investigations were carried out on the outer surface and cross section of the exposed sample using XRD, SEM/EDS and TEM. The analysis revealed the development of a fine grain oxide scale thickness spanning from 20 to 200 μm, consisting Fe_2NiO_4 (78 %), $Cr_{1.3}Fe_{0.7}O_3$, Fe_2O_3 (0.8 %) and Fe_3Co (0.8 %). Cross-sectional observations showed the formation of grains rich in Nb precipitates type MX carbonitrides surrounded by $M_{23}C_6$ carbides developed as a continuous net at the grain boundaries. The extent of material degradation under the influence of temperature, pressure and exposure time has been meticulously discussed.

Graphical Abstract

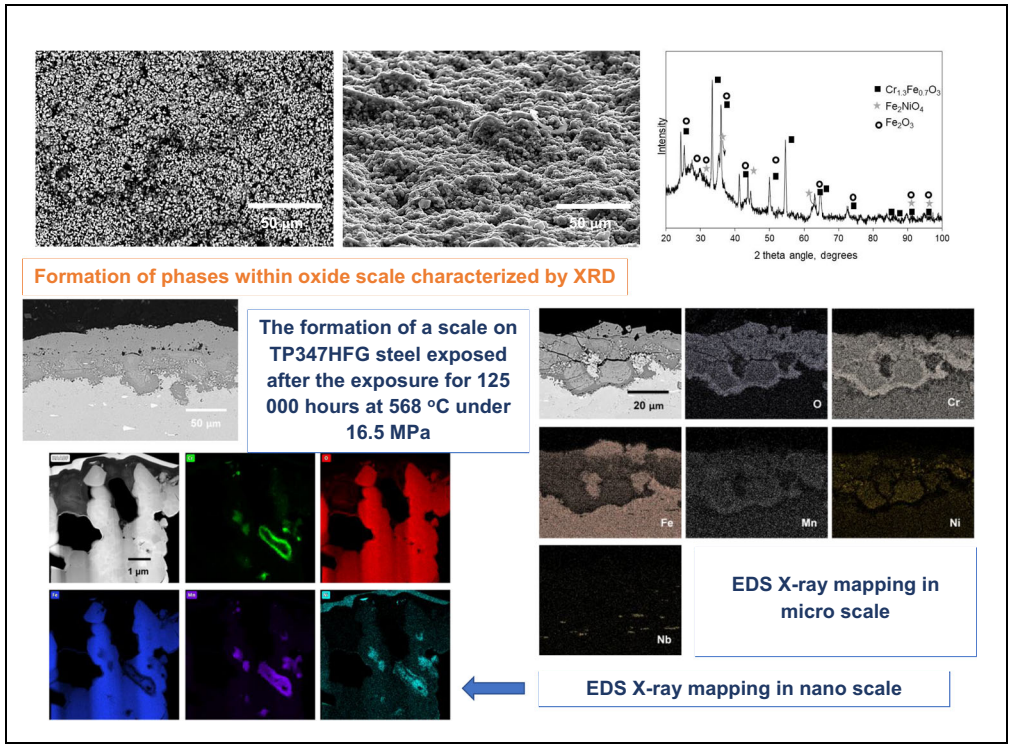

Tomasz Dudziak, Puneet Chandran, Karolina Chat-Wilk, and **Adelajda Polkowska**, Lukasiewicz Research Network-Krakow - Institute of Technology (KIT)—Centre of Materials and Manufacturing Research, Zakopiańska 73 Str., 30-418 Krakow, Poland; **Jerzy Morgiel**, Institute of Metallurgy and Materials Science of Polish Academy of Sciences, Reymonta 25 Str., 30-059 Krakow, Poland; and **Grzegorz Golański**, Faculty of Production Engineering and Materials Technology, Institute of Materials Engineering, Częstochowa University of Technology, Al. Armii Krajowej 19, 42-201 Częstochowa, Poland. Contact e-mail: tomasz.dudziak@kit.lukasiewicz.gov.pl.

Keywords austenitic steel, carbides, high-pressure steam, high temperature, oxidation

Published online: 19 August 2024

1. Introduction

The surge in operating parameters (steam pressure, temperature) of coal-fired power units facilitated increased thermal efficiency and reduced the negative impact on the natural environment due to lower CO_2 emission. The use of modern technologies such as super and ultra-super-supercritical (USC) steam parameters in coal power plants was possible with introduction of the modern steel grades with appropriate creep and high-temperature oxidation resistance at temperature ranges between 600 to 620 °C (Ref 1). It is well known that chromium (Cr) addition to steel matrix ensures high degree of steam oxidation resistance. At least 10.5% of Cr is needed to develop a stable passive layer of Cr oxide that significantly decelerates the steam oxidation process at high temperatures in comparison to a steel grade with a low Cr content (2-3 wt.%.) or no Cr content in metal matrix.

Higher working temperatures lead to accelerated oxidation of steel irrespective of the grades employed. Further, due to higher oxidation rates, the thickness of the oxide scale reaches a critical value ensuing an imminent flaking and falling off process. This flaky, less adherent oxide scale significantly contributes to the reduction in durability and performance of the structural elements of the power station (Ref 2, 3). The higher the Cr content in the steel, the better oxidation resistance and lower mass loss of the materials when exposed to high temperatures (Ref 3, 4). Austenitic steels due to their microstructure/ crystal structure and Cr content exhibits better oxidation resistance than ferritic steels used in the same operating conditions, therefore austenitic steels are preferred over ferritic steels to manufacture crucial infrastructure of power plants to sustain severe conditions related to high temperature, pressure, etc (Ref 2, 3). Variation in Cr content in the metal matrix of the exposed material is not the only factor enabling resistance at high temperatures, grain size, heat flux, aggressiveness of the environment, peroxidation treatment and surface treatment are multiple parameters which support the same case (Ref 5-8).

In most laboratories worldwide, high temperature oxidation tests in steam atmosphere are performed on steel grades delivered in their as-received state (i.e., after solution treatment). The results of such tests present mostly oxidation kinetics, oxidation rates under assumed condition to evaluate thickness of oxide scale formation in the exposed material (Ref 2, 5, 6). However, these laboratory-based tests do not always meet the criteria of real atmosphere present in power plants where high pressure and temperature often converge. In addition, due to long exposure times, some changes appear within the microstructure leading to negative consequences that involve reduction in oxidation resistance, i.e., due to the precipitations of the Cr-rich phases (Ref 9) or formation of the σ phase (Ref 10). Both these phases are responsible for the deterioration of stainless steels properties, for example, mechanical property, oxidation resistance and weldability.

Further, research initiatives pertaining to the characterization of the oxide structure and high-temperature oxidation resistance of austenitic steel, i.e., TP347HFG after long-term service (125 000 hrs) is very meager. Therefore, the underlying research objective of this paper is to determine and fully explore the nature of the oxide scale developed under high-pressure and elevated temperature using scanning electron microscope (SEM) coupled with energy-dispersive x-ray spectroscopy (EDS), x-ray diffraction (XRD) and finally transmission electron microscopy (TEM)

2. Material

The oxidized steel samples studied in this research were isolated from the material exposed for 125 000 hrs at 568 °C under 16.5 MPa steam pressure. The TP347HFG steel with chemical composition given in Table 1 had following dimensions: tube with 44.8 mm (OD) and wall thickness 8.6 mm.

The chemical composition analysis of the steel was performed using a Bruker Q4 Tasman spark spectrometer. The microstructural investigations were carried out using a JEOL JSM-6610LV and FEI Scios 2 SEM equipped with FEG filament working at 20 kV accelerating voltage in mode of a concentric back scattered (CBS) detector with working distance 10 mm. Jeol 2100 Plus transmission electron microscope (TEM) was used to study the oxide in nanoscale. The specimens for SEM microstructural analysis were prepared by grinding with SiC papers (up to 1200 SiC) followed by polishing with 0.1 μm Al_2O_3 paste from Struers and finally electrochemically etched using Mi19Fe agent and was observed under the microscope in an orientation perpendicular to the axis of the tube section. Thin foils for TEM microstructure characterization of the tube material were prepared in disc form ($\phi-$ 3 mm, thickness $\sim$ 100 μm). They were electrolytically thinned to near perforation using a solution of 20% perchloric acid in ethanol at a temperature of approx. $-$ 20 °C and voltage $\sim$ 20 V. The identification of precipitates on thin films was performed using selective electron diffraction. The microanalysis of the scale were performed using Themis probe corrected TEM equipped with SuperX EDS system. Maps presenting distribution of respective elements were acquired using 500×500 matrix. Specimens for these measurements were cut from the tube surface using FIB technique. The phase analyses of the oxidized TP347HFG steel was carried out using Panalytical Empyrean, PiXcel3D machine with ICDD PDF-4 + 2020 database. The specimen was scanned in the 2θ range of 20°-100°, using Co Kα radiation at a scanning rate of 1.5° min^{-1} with a 40 mA tube current and 40 kV voltage.

3. Results and Discussion

3.1 Surface Microstructure of the Steel After Service

Figure 1A, B shows the surface of the exposed material for 125 000 hrs at

568 °C and 16.5 MPa steam pressure. The SEM images were captured from different areas of the exposed material. The findings indicate continuous micro structure with similar morphology consisting of a fine grain of oxides with a diameter up to 0.5-0.7 μm.

Table 1 Chemical composition of the investigated steel (wt.%)

C	Si	Mn	P	S	Cr	Ni	Nb	N
0.11	0.38	1.45	0.027	0.002	18.5	12.2	0.54	0.11

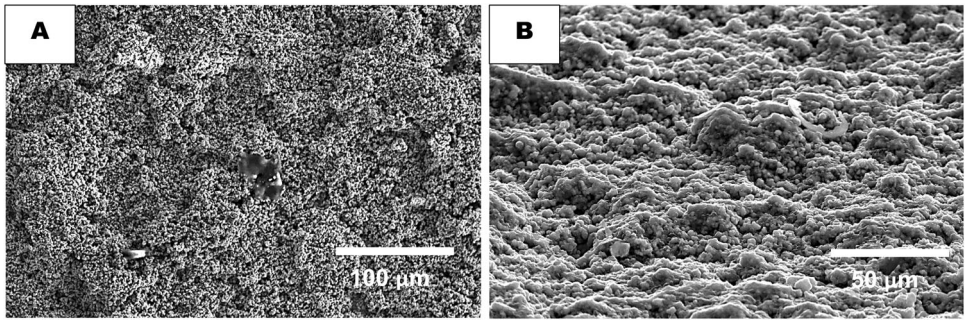

Fig. 1 SEM observations of the surface of the material exposed in real power plant steam conditions (125 000 hrs at 568 °C and 16.5 MPa)

Figure 2 shows the XRD phase analysis of the oxides developed on the surface. Figure 3 is a representative pie chart showing percentage share of the phases developed at the surface.

The results of the XRD analysis performed on the delivered samples indicate that the most favorable phase developed under service conditions was Fe_2NiO_4

(78 %), $Cr_{1.3}Fe_{0.7}O_3$ (19.9 %) and finally Fe_2O_3 (1.6%). The results clearly indicate the formation of complex phases within a long-term exposure at high temperature. The formation of spinel $Cr_{1.3}Fe_{0.7}O_3$ is a result of the excess Cr_2O_3 and reaction with

Fe_2O_3 (Ref 11, 12):

$$0.65Cr_2O_3 + 0.35Fe_2O_3 = Cr_{1.3}Fe_{0.7}O_3 \quad \text{(Eq 1)}$$

If the diffusion of Cr toward the surface is too slow (not enough diffusion paths, low activity of Cr), due to high activity and concentration of Fe in the metal matrix, Fe will oxidize first. Subsequently, the outermost layer is created due to the fast, outward diffusion of Fe. Due to the insufficient concentration and activity of Cr, it is internally oxidized through the inward diffusion of O_2. The formation of spinel Fe_2NiO_4 is related to diffusion of Ni through the Fe_2O_3 phase (Ref 13).

3.2 Cross-Sectional Analysis

The microstructure captured by SEM of the steel after the service is given in Figure 4. The studied steel was characterized by a fine grain structure (grain size 8 according to ASTM standard), with many different precipitations that were observed either within grains as well as in grain boundaries and twin boundaries.

On grain boundaries, the precipitates observed not only revealed formation of continuous net, but also the grain boundaries were affected by singular precipitates. Singular precipitates were also found on twin boundaries. Based on microstructure observations, inside the grain singular and colony of fine precipitates were spotted. In heat-resistant steel grades such as 347HFG stabilized by addition of Nb, a large precipitates rich in Nb are treated as primary precipitates that originate directly from a liquid, whereas secondary fine grain precipitates are derived from the matrix (Ref 14). The analysis carried out indicated the presence of $M_{23}C_6$ carbides on grain boundaries as shown in Figure 5. Internal architecture of the Nb-rich grains in precipitates type MX is shown in Figure 6. In the observed microstructure of the exposed steel, a large volume of twins were also observed.

The addition of Nb to austenitic steel in contrast to Cr is not related to improved oxidation resistance. Nb is added to the

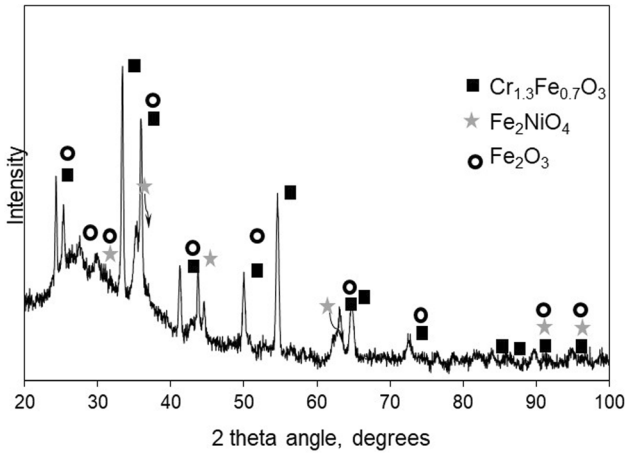

Fig. 2 XRD diffraction pattern of TP347HFG steel

austenitic steel to reduce the risk of intergranular corrosion and as a strengthening agent (higher creep resistance) in the form of Nb(C,N). Nb is a strong carbide forming element. The presence of strong carbide forming elements in chemical composition results in increased precipitates in the as-received state. The presence of NbC strongly reduced the formation of $M_{23}C_6$ carbides and formed the NbC (NbX) phase as primary and secondary precipitates. The large primary NbC (NbX) precipitates (size in μm) develop in the final stage of crystallization of the stabilized austenitic steels TP347HFG, therefore, often these phases were observed near or at the grain (Ref 15, 16). The TP347HFG steel belongs to a fine grain heat-resistant austenitic steels with a grain size of 8 according to ASTM. This fine grain structure originates from the dedicated heat treatment of the material (solution treating temperature between 1200 and 1250 °C) (Ref 17). As a result, heat treatment within the microstructure indicated the presence of dispersive particles inhibit grain growth. Thus, the as-received TP347HFG steel exhibited both primary precipitates and secondary precipitates as MX (Ref 17, 18). According to Erneman et al., the precipitates show a high degree of thermodynamical stability (Ref 18) ensuring good mechanical properties (Ref 19). The presence of numerous twins in the steel microstructure as a result of hot deformation and final solution treatment is characteristic of Fe-based alloys with A1 structure and originates from a low stacking fault energy. The twins that are present in the austenitic steels structure are not only vital for mechanical properties, but also significantly reduce intergranular corrosion degradation (Ref 20, 21).

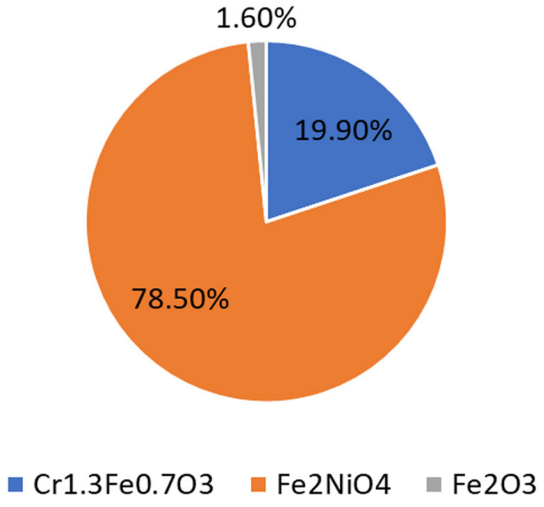

Fig. 3 Percentage volume of phases on the surface of TP347HFG steel

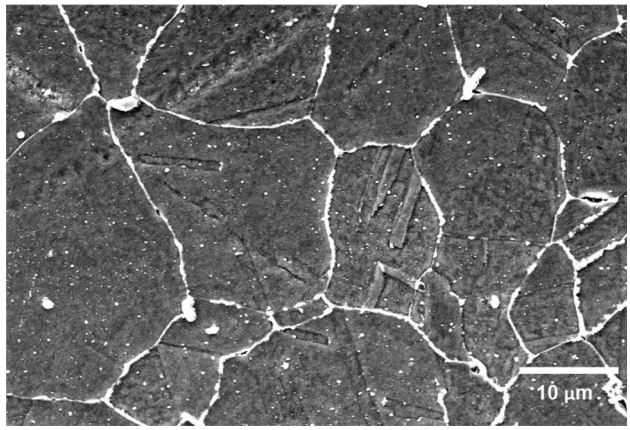

Fig. 4 The microstructure of the cross-sectional steel after the service in real power plant conditions showing a grid of precipitates on the grain boundaries, SEM

Precipitation processes are responsible for degradation of the microstructure of the austenitic steels during the exposure. The most favorable spots for formation of precipitations are gain boundaries with a high surface energy (500-600 mJ/m^2) (Ref 22).

This is due to the fact that, in grain boundaries surface defects allow faster diffusion of alloying elements in contrast to diffusion within the grain which is relatively more demanding. As shown in Figure 5A, $M_{23}C_6$ phase was formed on the grain boundaries as singular precipitates in the form of a continuous net. The formation of precipitates rich in Cr such as $M_{23}C_6$ in austenitic steels is related to the limited solubility of C in austenite phase. The high number of precipitates observed at the grain boundaries is probably due to their intrinsic nature where nucleation and growth occurred. The grain boundaries in austenitic steels with a high degree of coincidence Σ or grain boundaries with a wide misorientation angle Θ are favorable spots for $M_{23}C_6$ precipitation (Ref 23, 24). Hu et al. (Ref 25) found that at a low misorientation angle Θ and when $\Sigma \leq 9$ due to low interfacial energy, no $M_{23}C_6$ phase was observed. The contrast to MX precipitates leads to coagulation of the former and developing a continuous net of $M_{23}C_6$ precipitates as shown in Figure 4 and 5A (Ref 26). The lower boundary surface energy of twins in austenitic steel, noncoherent (100-500 mJ/m^2) and coherent (20 mJ/m^2) is instrumental for nucleation and particle growth along the twin boundary which is lower at the grain boundaries (Ref 22). Thus, grain boundaries revealed only a singular precipitates as shown in Figure 4.

Figure 7A, B presents the cross-sectional images of the microstructure including the oxide scale that formed during the exposure of the TP347HFG steel.

The SEM images depict the usual microstructure of the material exposed in real power plant conditions. The oxide scale showed random thickness ranging from 20 μm to 200 μm. According to XRD analyses, the oxide scale consisted Fe_2NiO_4, $Cr_{1.3}Fe_{0.7}O_3$ Fe_2O_3 and Fe_3Co. The oxide scale also showed void formation on the border between outer oxide scale and the inner oxide scale. The growth process of the oxide scale can occur either by metal or oxidant diffusion or both ways. The involvement of metal/oxidant diffusion in the overall transport process through the oxide scale depends on the type of crystal lattice defects present in the oxidation product. The oxide scale developed for over 125 000 hrs indicate slightly different phase constituents in line with the experimental finding reported by Wright and Dooley (Ref 27). They indicated that fine-grained 347HFG grade steel developed equal parts of Fe_3O_4 and Fe_2O_3 after 11 000 hrs exposure at 670 °C, whereas the two layer Fe–Cr spinel oxide scale had a decreasing chromia level from the inner most layer toward the surface. However in this study, the outer layer consisted only of Fe_2O_3 and no other phase was found which could be attributed to harsh oxidation working parameters used. Montgomery et al (Ref 28) also reported the formation of a double-layered oxide in fine-grained TP347HFG after 30000 hrs in steam of which the outer layer was occupied by magnetite.

The mechanism of the scale formation at high temperature under steam is very complex in nature, during the exposure multiple mechanisms may act at the same time, therefore it is not always clear which mechanism predominates under dynamic steam oxidation process. According to Fujii et al.(Ref 29), the following mechanisms that induce high-temperature degradation may be considered.

- Dissociation mechanism
- Oxidant-gas penetration mechanism
- Formation and volatilization of $Fe(OH)_2$
- Formation and volatilization of $CrO_2(OH)_2$
- Changes in the oxide defect structure via proton dissolution

In the dissociation mechanism, metal ions that are generated from reactions at interfaces migrate to the outer interface of the oxide scale, and the rich pO_2 atmosphere where water vapor is adsorbed. Subsequent reaction forms wustite (FeO), defects in the oxide and adsorbed hydrogen. Most of the hydrogen is believed to desorb, but some will dissolve in the oxide. However, this mechanism is not completely related to the current study, since wustite (FeO) at temperature below

570 °C is not stable (Ref 30). On the other hand, the investigated steel material in this work was exposed for a long-term service at temperature 568 °C, therefore, the border line of wustite could be attained and the phase could form. However, this mechanism is not the most predominating (Ref 31, 32).

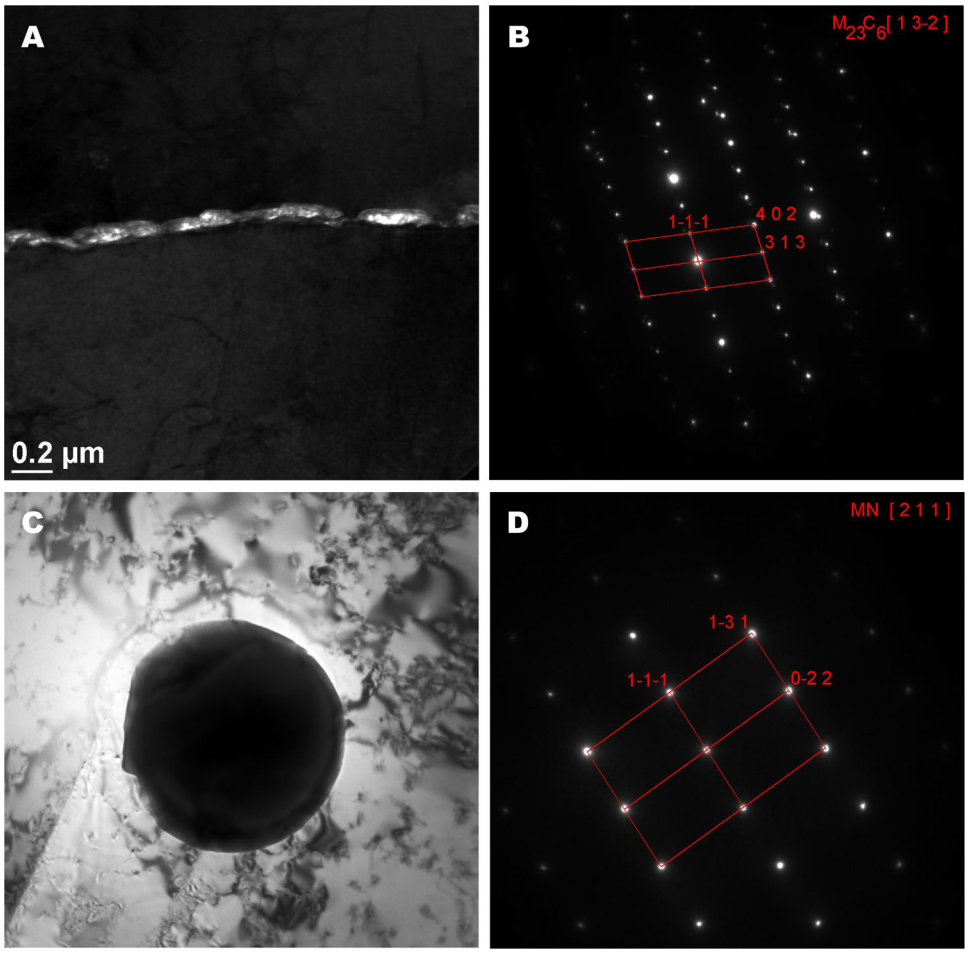

Fig. 5 Particles identified in the investigated steel: (A, B) $M_{23}C_6$ carbide, (C, D) primary MN type precipitate, TEM

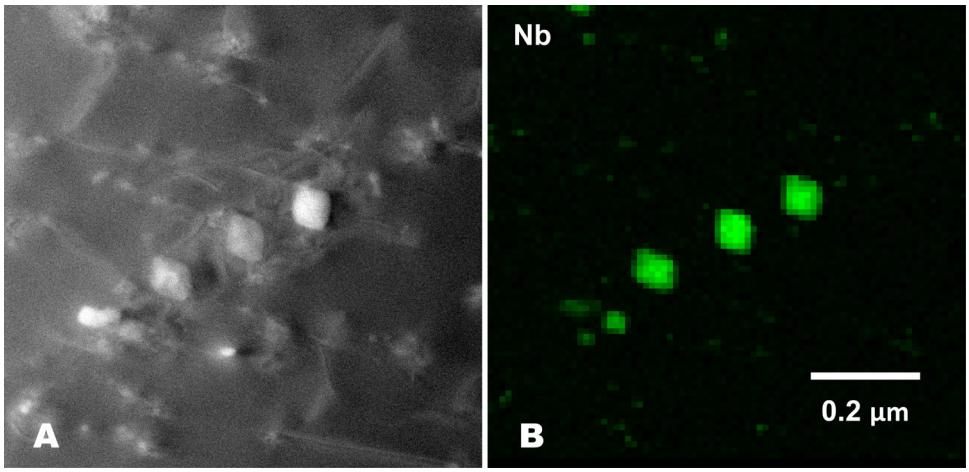

Fig. 6 The MX Nb-rich precipitates inside grains (A); map of elements distribution: (B) Nb; TEM

Later studies regarding degradation of high Cr austenitic steels, involved the formation and volatilization of $Fe(OH)_2$ phase due to the sequence of reactions in steam (Ref 33), processes such as outward diffusion of iron cations to the oxide/gas interface, inward diffusion of oxygen anions to the metal/oxide interface and vapor-phase diffusion of $Fe(OH)_2$ to the oxide/gas interface. Finally, degradation of the exposed steel in a long-term service can be related as well to the Cr volatilization during the exposure. When a Cr containing steel is exposed then, the presence of H_2O may increase the evaporation loss by

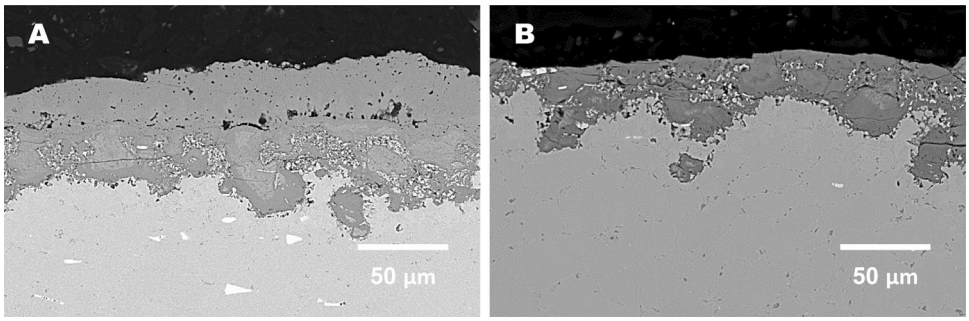

Fig. 7 SEM cross-sectional images of the TP347HFG steel microstructure developed in real conditions of power plant under 16.5 MPa at 568 °C for 125 000 hrs

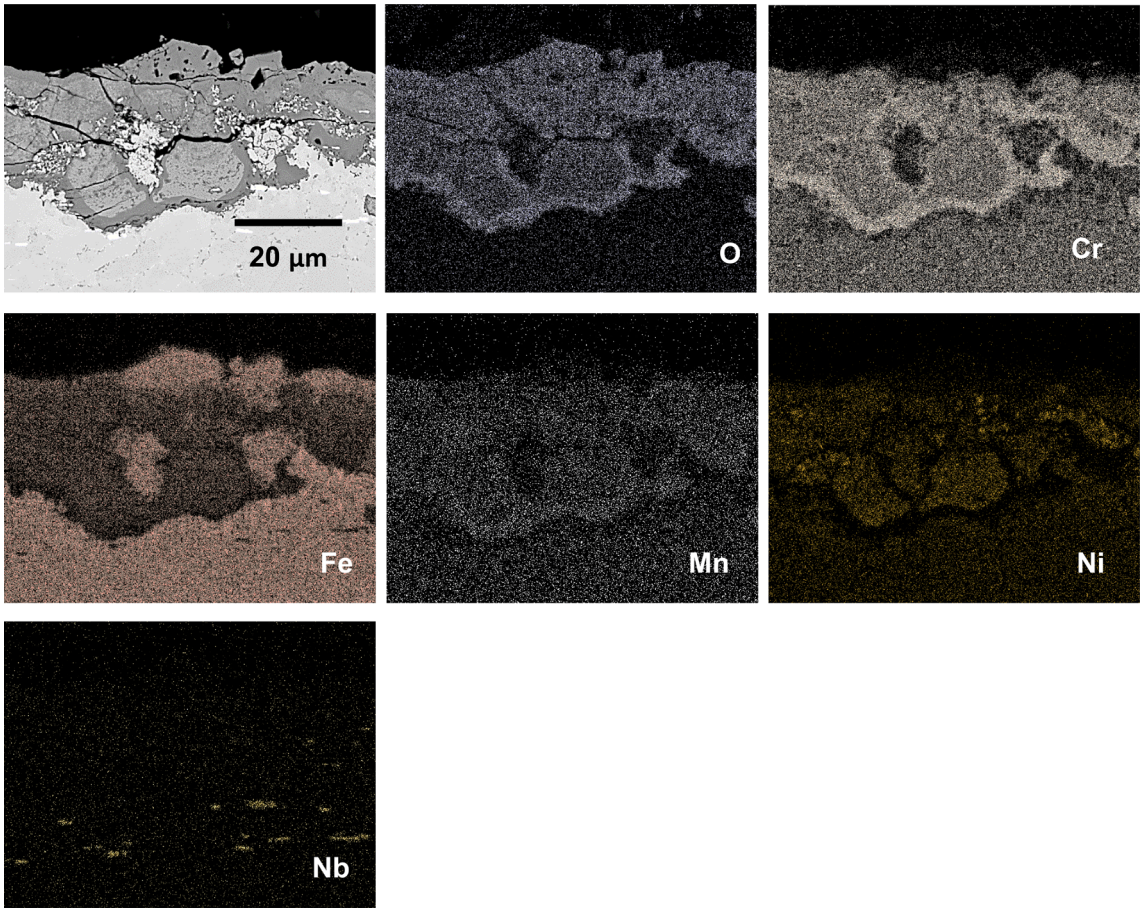

Fig. 8 SEM cross-sectional x-ray mapping of the TP347HFG steel microstructure developed in real conditions of power plant under 16.5 MPa at 568 °C for 125 000 hrs

allowing the formation of $CrO_2(OH)_2$ phase, which has a higher vapor pressure than CrO_3. The reaction of $CrO_2(OH)_2$ phase formation is given below:

$$\frac{1}{2}Cr_2O_3 \downarrow + H_2O + \frac{3}{4}O_2 \uparrow = CrO_2(OH)_2 \uparrow \qquad \text{(Eq 2)}$$

The process of decomposition changes overall kinetic reaction leading to linear rate of the oxide scale growth (chemical reaction controlled) from a parabolic rate growth (diffusion controlled). Also, this mechanism rapidly changes thickness of the scale leading to spallation of the scale due to lack of adherence when critical thickness is reached. A significant loss of Cr by volatilization is not expected in this particular case to play a major role in the breakdown of protective scales in steam due to the lower prevailing oxygen partial pressure. Significant loss of Cr via volatilization in steam is expected at the higher temperatures and pressures associated with ultra-supercritical steam cycles (740 °C, 30 MPa) (Ref 34).

Figure 8 shows EDS x-ray mapping of the TP347HFG steel after exposure in power plant. The performed analysis indicates the formation of the rich Fe, Cr, O rich scale with additional presence of Ni.

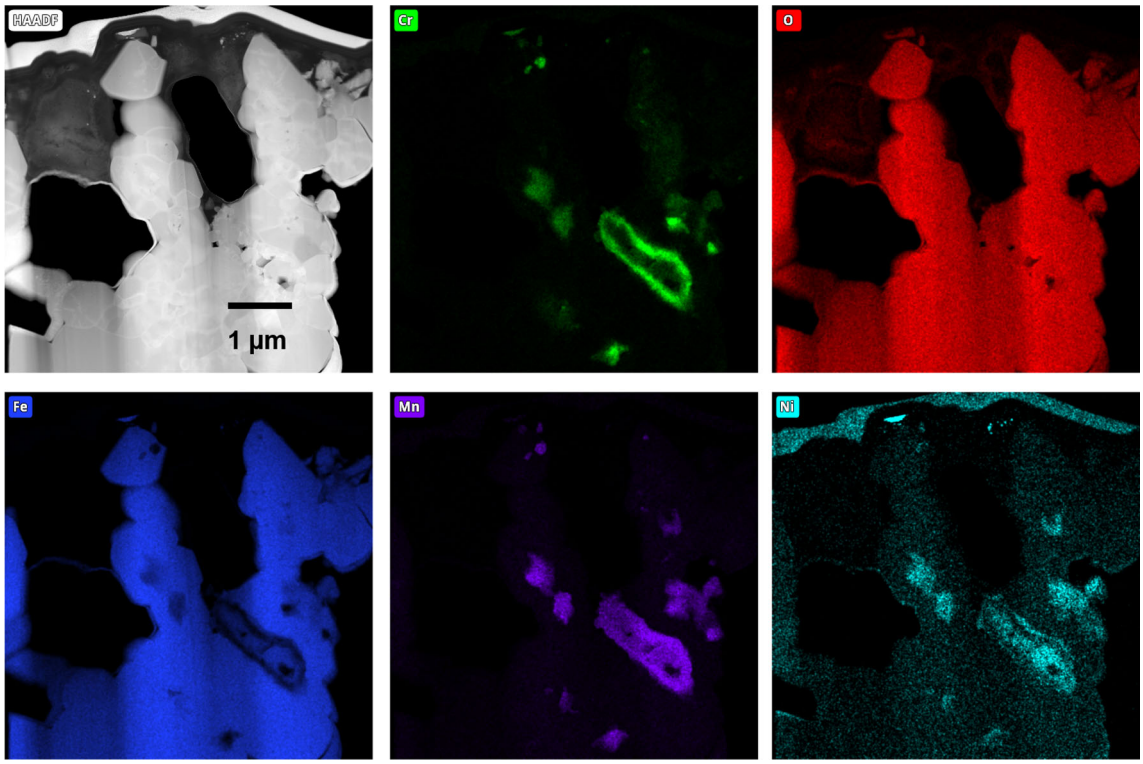

Fig. 9 TEM cross-sectional x-ray mapping of the TP347HFG steel microstructure developed in real conditions of power plant under 16.5 MPa at 568 °C for 125 000 hrs

The EDS x-ray mapping shows the presence of Mn; however, this finding is in contrast to XRD where no Mn phase was observed from the surface of the sample. The Mn containing phase could be present as a $MnCr_2O_4$ phase, whose concentration is under the detection threshold of XRD or the phase was largely dispersed within the oxide scale, hence its absence in the XRD analysis. Also, between the oxide scale and the substrate a Cr, O enriched region was formed suggesting Cr_2O_3 phase formation. The presence of Cr_2O_3 phase at the interface is greatly beneficial which acts as a barrier for the further ingress of oxygen from the steam atmosphere due to inward diffusion of O^{2-} ions. Within this enriched Cr zone, Mn also showed a higher concentration indicating presence of $MnCr_2O_4$ as well. The presence of this phase further increases the diffusion barrier. According to Holcomb et al., Mn in Ni-Cr alloys is added to reduce Cr volatilization process at high temperatures and high pressures. It was postulated, that Mn additions to Cr-rich Ni-based alloys decreases the activity of Cr within the oxide, either from solid solution replacement of Cr with Mn (at low levels of Mn) or from the formation of Mn-Cr spinels (at high levels of Mn). This reduction in Cr activity leads to a predicted reduction in Cr evaporation by as much as a factor of 35 at 800 °C and 55 at 700 °C (Ref 35). It is strongly believed, that addition of Mn to rich Cr, Fe-based alloys has a similar effect as in Ni-based alloys.

The TEM observations were used in this study to have a closer look at the happenings and show the microstructure of the external part of the oxide scale developed at high temperature for 125 000 hrs in steam pressure of 16.5 MPa. The results are presented in Figure 9.

The white band on TEM image shows Ni layer that is used to stabilize the oxide scale during processing. The TEM images reflect a high degree of porosity of the columnar oxide developed. As observed, the external part of the oxide scale is rich in Fe and O suggesting a high concentration of Fe_2O_3 phase, as opposed to the minor quantities of Fe_2O_3 observed in the XRD analyses. The overlapping presence of Cr and Mn suggested the formation of $MnCr_2O_4$ spinel phase. The Ni presence was confirmed as well during the mapping investigations performed on TEM analyses. Elemental mappings confirmed the presence of Ni in a deeper part of the oxide scale in the same places as Cr and Ni; however, a higher concentration of Cr, Mn, Ni elements are randomly distributed within the oxide scale instead of continuous layer of the oxide scale as shown in Figure 10.

To understand the broader implications of the findings in the current study, a few relevant studies have been discussed and correlated. For higher operating temperatures and conditions in supercritical water, such material may not be suitable (374 °C, 22.1 MPa) (Ref 36). The mechanism of steam oxidation of 310 SS with as high as 20 wt.% Cr lead to the development of a structure with an outer, inner and thin Cr_2O_3 layer. The outer layer according to the authors was grown by solid state mechanism but the inner layer was developed by internal oxidation and transition mechanism from internal to external oxidation at the oxidation front. Similar to the current work with 347HFG steel, the exposure of 310SS showed the formation not only of a thin Cr_2O_3 but also an external oxide scale consisting Fe_2O3, $NiFe_2O_4$ and NiO, whereas the internal part was rich in Fe-Cr-Ni spinel. In current study, this situation was not observed, EDS mapping carried out on 347HFG steel showed enrichment of Cr between the oxide scale and the substrate, but this enriched band was also occupied by other elements (Ni, Fe).

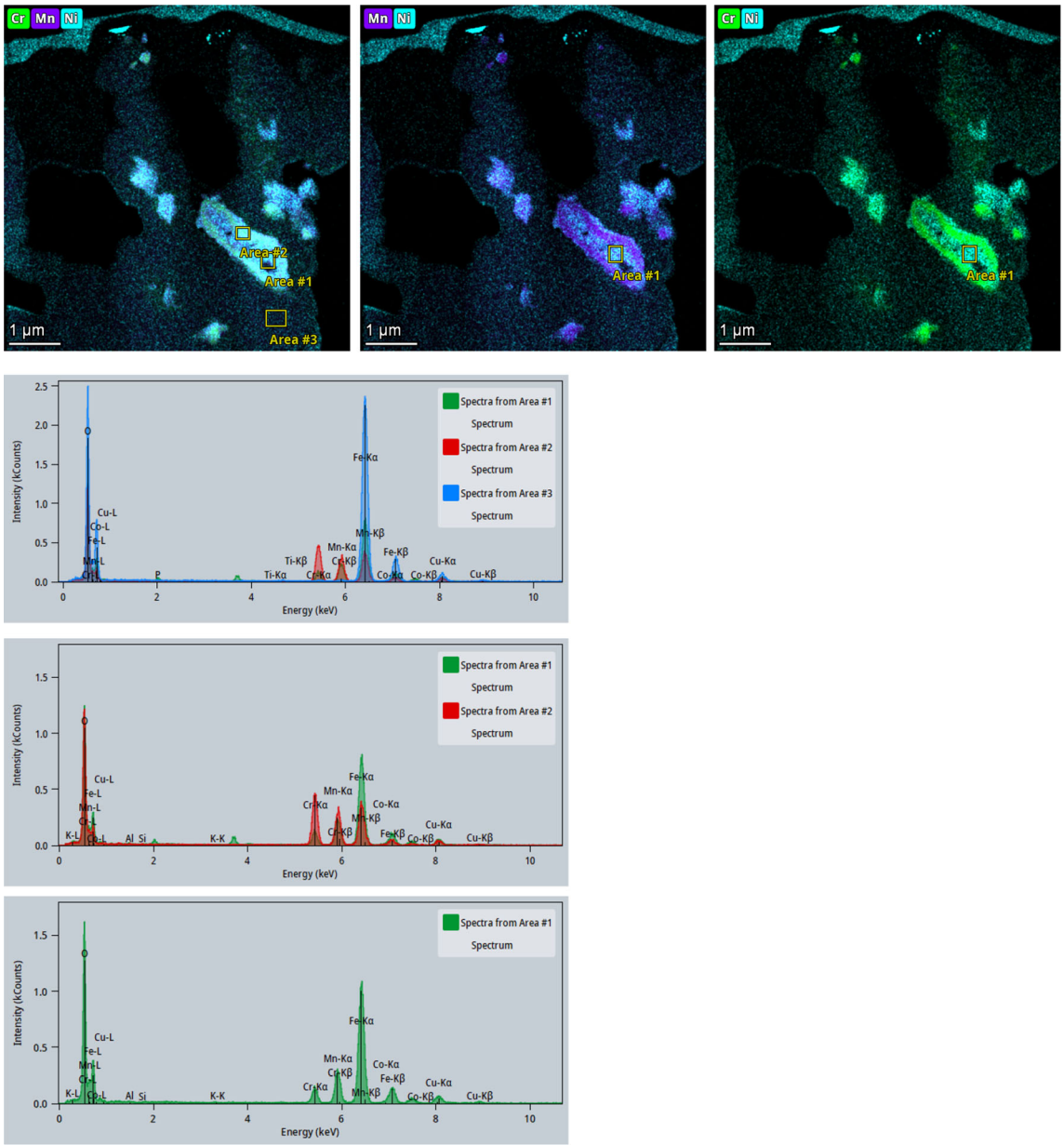

Fig. 10 The elemental mappings with EDS data of the elements with the highest concentrations (O, Fe, Ni, Cr, Mn)

Zhao and coauthors studied oxidation resistance of the steels using advanced techniques to provide a new insight into the oxidation process of the materials with different Cr concentration. Ferritic martensitic steels with a Cr concentration between 9 and 12 wt.% were studied in deaerated high-temperature steam at 600 °C for 100 hours (Ref 37). According to these findings, the exposed material developed triplex not duplex oxide scale. Often researchers in the past indicated a duplex oxide scale formation (Ref 2, 38, 39) as a model oxide scale for steels with higher than 9 wt.% Cr in metal matrix. Duplex oxide scale was described using following approaches: the mechanism of scale dissociation (Ref 40), different diffusion coefficient of Fe and Cr (Ref 41). The third approach is where simultaneous diffusion of oxidant and cations is responsible for the oxide scale formation (outer and inner).

Nevertheless, abovementioned theories are in contrast to the work presented by authors (Ref 37). The formation of a triplex oxide scale, including an outer oxide layer, an inner oxide layer and an internal oxide layer is a new phenomenon according to the authors. Based on this finding, it can be deducted that nonreactive metal phases could form as a result of very low pO_2 between those two layers. In line with this study, 347HFG steel exhibited columnar outer oxide layer as a result of outward diffusion of Fe from the inner and internal oxide layers giving limited protection to the metal matrix.

Zhao et al (Ref 42) studied the microstructure and chemistry of the oxide scales formed on Fe-21Cr-32Ni and Fe-17Cr-9Ni steels. The materials were exposed to deaerated high-temperature high-pressure steam at 600 °C for 1500 hours. They found that the steel with a higher Cr content was initially internally oxidized, and then an external oxide scale was developed together with an inner Cr-rich band under the internal oxidation zone. In the Fe-17Cr-9Ni steel, similar chemical composition to 347HFG steel was internally oxidized together with an external

Fe-rich oxide scale during the entire experimental period, which is also observed in the 347HFG steel.

4. Conclusions

The aim of this paper was to analyze the sample of 347HFG steel exposed for 125 000 hrs at 568 °C under 16 MPa pressure. Based on the analysis carried out, the following conclusions are made:

- The exposed TP347HFG steel indicated a high degree of steam oxidation degradation due to the formation of a thick scale ranging from 25 to 200 μm.
- A porous scale developed with horizontal cracks within the formed oxide scale along with a protective Cr_2O_3/$MnCr_2O_3$ band formed at the oxide scale–substrate interface.
- The oxide scale formed consisted mainly Fe_2NiO_4, (78 %), $Cr_{1.3}Fe_{0.7}O_3$, Fe_2O_3 (0.8 %) and Fe_3Co (0.8 %).
- $MnCr_2O_4$ spinel phase which was undetected by XRD, but evidenced by SEM and TEM elemental mapping.
- The formation of continuous net type $M_{23}C_6$ carbides at grain boundaries, singular particles at twins boundaries apart from coarse and fine Nb (C,N) particles inside grains were found after a long service time as key precipitates in the steel microstructure.

References

1. J.P. Patil, M. Paliwal and S.K. Mishra, A Review on the Material Development and Corresponding Properties for Power Plant Applications, *Mater. Perfor. Charact.*, 2022, **11**, p 53–87. https://doi.org/10.1520/MPC20200173
2. I.G. Wright and R.V. Dooley, Morphologies of Oxide Growth and Exfoliation in Superheater and Reheater Tubing of Steam Boiler, *Mater. High Temp.*, 2011, **28**, p 40–57. https://doi.org/10.3184/096034011X12982937656387
3. T. Dudziak, M. Lukaszewicz, N.J. Simms, and J.R. Nicholls, Impact Specimen Geometry on T23 and TP347HFG Steels Behaviour During Steam Oxidation at Harsh Conditions, *Corros. Eng. Sci. Technol.*, 2016, **6**, p 46–53. https://doi.org/10.1080/1478422X.2016.1185568
4. S.R.J. Saunders, M. Monteiro, and F. Rizzo, The Oxidation Behaviour of Metals and Alloys at High Temperatures in Atmospheres Containing Water Vapour: A Review, *Prog. Mater. Sci.*, 2008, **53**, p 775–837. https://doi.org/10.1016/j.pmatsci.2007.11.001
5. Z.W. Yue, M. Fu, X.G. Wang, and X.G. Li, Effect of Shot Peening on the Oxidation Resistance of TP304H and HR3C Steels in Water Vapor, *Oxid. Met.*, 2012, **77**, p 17–26. https://doi.org/10.1007/s11085-011-9270-6
6. M. Lukaszewicz, N.J. Simms, T. Dudziak, and J.R. Nicholls, Effect of Steam Flow Rate and Sample Orientation on Steam Oxidation of Ferritic and Austenitic Steels at 650 and 700 °C, *Oxid. Met.*, 2013, **79**, p 473–483. https://doi.org/10.1007/s11085-013-9358-2
7. Z.Y. Liang and Q.X. Zhao, Steam Oxidation of Austenitic Heat-Resistant Steels TP347H and TP347HFG at 650–800 °C, *Materials*, 2019, **12**, p 577. https://doi.org/10.3390/ma12040577
8. J.T. Yuan, X.M. Wu, W. Wang, S.L. Zhu, and F.H. Wang, The Effect of Surface Finish on the Scaling Behavior of Stainless Steel in Steam and Supercritical Water, *Oxid. Met.*, 2013, **79**, p 541–551. https://doi.org/10.1007/s11085-013-9380-4
9. G. Golański, A. Zieliński, M. Sroka, and J. Słania, The Effect of Service on Microstructure and Mechanical Properties of HR3C Heat-Resistant Austenitic Stainless Steel, *Materials*, 2020, **13**, p 1297. https://doi.org/10.3390/ma13061297
10. C.-C. Hsieh and W. Wu, Overview of Intermetallic Sigma (σ) Phase Precipitation in Stainless Steels, *Int. Sch. Res. Netw. ISRN Metal.*, 2012 https://doi.org/10.5402/2012/732471
11. J. Tang, M.S. Chu, C. Feng, F. Li, and Z.G. Liu, Phases Transition and Consolidation Mechanism of High Chromium Vanadium-Titanium Magnetite Pellet by Oxidation Process, *High Temp. Mater. Proc.*, 2016, **35**(7), p 729–738. https://doi.org/10.1515/htmp-2015-0067
12. S.X. Wang, L.S. Cui, G.Q. Wang, Y.J. Zheng, H.X. Wang, and J.S. Jia, Properties of Oxide Films Grown on 25Cr20Ni Alloy in Air-H_2O and H_2–H_2O Atmospheres, *Pet. Sci.*, 2014, **11**, p 147–154. https://doi.org/10.1007/s12182-014-0326-5
13. B. Rutkowski, K. Baran, R. Błoniarz, and T. Kozieł, Microstructural Investigation of Austenitic Heat Resistant Alloy after 500 h of Steam Oxidation, *Materials*, 2021, **14**, p 1453. https://doi.org/10.3390/ma14061453
14. J. Erneman, M. Schwind, H.O. Andrén, J.O. Nilsson, A. Wilson, and J. Ågren, The Evolution of Primary and Secondary Niobium Carbonitrides in AISI 347 Stainless Steel During Manufacturing and Long-Term Ageing, *Acta Mater.*, 2006, **54**, p 67–76. https://doi.org/10.1016/j.actamat.2005.08.028
15. J.C. Rosser, M.I. Bass, C. Cooper, T. Lant, P.D. Brown, B.J. Connolly, and H.E. Evans, Steam Oxidation of Super 304H and Shot-Peened Super 304H, *Mater. High Temp.*, 2012, **29**(2), p 95–106. https://doi.org/10.3184/096034012X13316633785757
16. A. Zielinski, T. Dudziak, G. Golanski, J. Gazdowicz, and A. Kołodziej, Effects of Longterm Ageing at High Temperatures on Oxide Scale Development and Evolution of Austenitic Steels Microstructure, *Steel Res. Int.*, 2020, **91**(6), p 1900595. https://doi.org/10.1002/srin.201900595
17. K. Yoshikawa, H. Teranishi, K. Tokimasa, H. Fujikawa, M. Miura, and K. Kubota, Fabrication and Properties of Corrosion Resistant TP347H Stainless Steel, *J. Mater. Eng.*, 1988, **10**, p 69–83. https://doi.org/10.1007/BF02834116
18. J. Erneman, M. Schwind, H.-O., andren, J.-O. Nilsson, A. Wilson and J. Ågren, The Evolution of Primary and Secondary Niobium Carbonitrides in AISI 347 Stainless Steel During Manufacturing and Long-Term Ageing, *Acta Mater.*, 2006, **54**, p 67–76.
19. G. Golański, A. Zieliński, and M. Sroka, Microstructure and Mechanical Properties of TP347HFG Austenitic Stainless Steel After Long-Term Service, *Int. J. Press. Vessels Pip.*, 2020, **188**, 104160. https://doi.org/10.1016/j.ijpvp.2020.104160
20. Y. Li and X. Wang, Precipitation behavior in boundaries and its influence on impact toughness in 22Cr25Ni3W3CuCoNbN steel during short-term ageing, *Mater. Sci. Eng. A*, 2021, **809A**, p 140924. https://doi.org/10.1016/j.msea.2021.140924
21. A.Y. Chen, W.F. Hu, D. Wang, Y.K. Zhu, P. Wang, H. Yang, X.Y. Wang, J.F. Gu, and J. Lu, Improving the Intergranular Corrosion Resistance of Austenitic Stainless Steel by High Density Twinned Structure, *Scripta Mater.*, 2017, **13**, p 264–268. https://doi.org/10.1016/j.scriptamat.2016.11.032
22. Y. Li and X. Wang, Precipitation Behavior in Boundaries and Its Influence on Impact Toughness in 22Cr25Ni3W3CuCoNbN Steel During Short-Term Ageing, *Mater. Sci. Eng. A*, 2021, **809A**, p 140924.
23. Y. Zhou, K.T. Aust, U. Erb, and G. Palumbo, Effects of Grain Boundary Structure on Carbide Precipitation in 304L Stainless Steel,

Scripta Mater., 2001, **45**, p 49–54. https://doi.org/10.1016/S1359-6462(01)00990-3
24. R. Jones, V. Randle, and G. Owen, Carbide Precipitation and Grain Boundary Plane Selection in Overaged Type 316 Austenitic stainless Steel, *Mat. Sci. Eng. A Struct.*, 2008, **496**, p 256–261. https://doi.org/10.1016/j.msea.2008.05.028
25. R. Hu, G. Gai, J. Li, J. Zhang, T. Zhang, and H. Fu, Precipitation Behavior of Grain Boundary $M_{23}C_6$ and Its Effect on Tensile Properties of Ni-Cr-W Based Superalloy, *Mater. Sc. Eng.*, 2012, **548A**, p 83–88. https://doi.org/10.1016/j.msea.2012.03.092
26. J. Vivas, D. De-Castro, E. Altstadt, M. Houska, D. San-Martín, and C. Capdevila, Design and High Temperature Behavior of Novel Heat Resistant Steels Strengthened by High Density of Stable Nanoprecipitates, *Mater. Sci. Eng. A*, 2020, **793**, 139799. https://doi.org/10.1016/j.msea.2020.139799
27. I.G. Wright and R.B. Dooley, A Review of the Oxidation Behaviour of Structural Alloys in Steam, *Int. Mater. Rev.*, 2010, **55**(3), p 129–167. https://doi.org/10.1179/095066010X12646898728165
28. M. Montgomery, O.H. Larsen, S.A. Jensen, and O. Biede, Field, Investigation of Steamside Oxidation for TP347H, *Mater. Sci. Forum*, 2004, **461–464**, p 1007–1014. https://doi.org/10.4028/www.scientific.net/MSF.461-464.1007
29. C.T. Fujii and R.A. Meussner, The Mechanisms of the High-Temperature Oxidation of Iron-Chromium Alloys in Water Vapour, *J. Electrochem. Soc.*, 1964, **111**, p 1215. https://doi.org/10.1149/1.2425963
30. V.B. Trindade, R. Borin, B. Zandi Hanjari, S. Yang, U. Krupp, and H.-J. Christ, High-Temperature Oxidation of Pure Fe and the Ferritic Steel 2 25Cr1Mo, *Mat. Res.*, 2005, **8**(4), p 365–369. https://doi.org/10.1590/S1516-14392005000400002
31. Y. Ikeda and K. Nii, Mechanism of Accelerated Oxidation on Fe-Cr Alloys in Water Vapour-Containing Atmospheres, *Corros. Eng.*, 1982, **31**, p 156. https://doi.org/10.3323/jcorr1974.31.3_156
32. Y. Ikeda and K. Nii, Microcrack Generation and its Healing in the Oxide Scale Formed on Fe-Cr Alloys, *Oxid. Met.*, 1978, **12**, p 487. https://doi.org/10.1007/BF00603806
33. P.L. Surman, The Oxidation of Iron at Controlled Oxygen Partial Pressures: I – Hydrogen/Water Vapour, *Corros. Sci.*, 1973, **13**, p 113. https://doi.org/10.1016/0010-938X(73)90023-1
34. D.J. Young and B.A. Pint, Chromium Volatilization Rates from Cr_2O_3 Scales into Flowing Gases Containing Water Vapor, *Oxid. Met.*, 2006, **66**(3/4), p 137–153. https://doi.org/10.1007/s11085-006-9030-1
35. G.R. Holcomb and D.E. Alman, Effect of Manganese Addition on Reactive Evaporation of Chromium in Ni-Cr Alloys, *J. Mater. Eng. Perform.*, 2006, **15**(4), p 394–398. https://doi.org/10.1361/105994906X117170
36. K. Chen, L. Zhang, Z. Shen, and X. Zeng, Revealing the Oxidation Mechanism of 310S Stainless Steel in Supercritical Water via High-Resolution Characterization, *Corros. Sci.*, 2022, **200**, 110212. https://doi.org/10.1016/j.corsci.2022.110212
37. Z. Shen, K. Chen, H. Yu, B. Jenkins, Y. Ren, N. Saravanan, G. He, X. Luo, P.A.J. Bagot, M.P. Moody, L. Zhang, and S. Lozano-Perez, New Insights into the Oxidation Mechanisms of a Ferritic-Martensitic Steel in High-Temperature Steam, *Acta Mater.*, 2020, **194**, p 522–539. https://doi.org/10.1016/j.actamat.2020.05.052
38. I.G. Wright and R.B. Dooley, A Review of the Oxidation Behaviour of Structural Alloys Insteam, *Int. Mater. Rev.*, 2010, **55**, p 129–167.
39. F. Rouillard, G. Moine, L. Martinelli, and J.C. Ruiz, Corrosion of 9Cr Steel in CO2 at Intermediate Temperature I: Mechanism of Void-Induced Duplex Oxide Formation, *Oxid. Met.*, 2012, **77**, p 27–55.
40. L. Martinelli, F. Balbaud-Celerier, A. Terlain, S. Delpech, G. Santarini, J. Favergeon, G. Moulin, M. Tabarant, and G. Picard, Oxidation Mechanism of a Fe-9Cr-1Mo Steel by Liquid Pb-Bi Eutectic Alloy (Part I), *Corros. Sci.*, 2008, **50**, p 2523–2536.
41. A. Atkinson, Surface and Interface Mass Transport in Ionic Materials, *Solid State Ion.*, 1988, **28–30**, p 1377–1387.
42. Z. Shen, J. Zhang, S. Wu, X. Luo, B.M. Jenkins, M.P. Moody, S. Lozano-Perez, and X. Zeng, Microstructure Understanding of High Cr-Ni austenitic Steel Corrosion in High-Temperature Steam, *Acta Mater.*, 2022, **226**, p 117634. https://doi.org/10.1016/j.actamat.2022.117634